Sustainable Energy & Fuels

ROYAL SOCIETY OF CHEMISTRY

PAPER

Published on 15 September 2026
Licensed under CC-BY 4.0

Check for updates

Cite this: *Sustainable Energy Fuels*, 2026, **10**, 4881

Hydrothermally preorganized wood-derived graphite with local single-crystal-like domains for coating-free lithium-ion battery anodes

Preethi Perianayagam, [a] Edwin Osebe Nyangau, [a] Futa Imaizumi,[a] Naoka Nagamura,[bc] Hideharu Niwa, [de] Takashi Itoh,[f] Masaru Watanabe[a] and Yuta Nakayasu *[af]

Fe-assisted graphitization offers a route to convert renewable biomass into graphite, but high crystallinity and fast electrochemical kinetics are difficult to achieve simultaneously at reduced temperature. Here, we show that a short hydrothermal carbonization step can function as precursor architecture engineering rather than simple wet pretreatment. $Fe(NO_3)_3$-impregnated Japanese cedarwood was hydrothermally treated for only 15 min at 250 °C to generate an iron–carbon hydrochar precursor in which mixed iron oxide domains, including Fe_3O_4, are embedded within a reactive carbon matrix. During annealing at 1000 °C, these reducible iron oxide domains are converted into Fe/Fe_3C catalytic interfaces that promote graphitic layer growth. After acid washing and mild air oxidation, the product exhibits graphite-like stacking with $d_{002} \approx 0.3369$ nm, low Raman disorder ($I_D/I_G = 0.14$), and a Raman-derived in-plane domain size of *ca.* 135 nm. HRTEM and SAED further revealed extended graphitic fringes and local single-crystal-like graphite domains within a polycrystalline sheet network. As a lithium-ion battery anode, the material, used without a post-synthetic surface coating, delivers 341/317 mAh g^{-1} lithiation/delithiation capacities at 1C and exhibits reproducible lithiation behavior within each rate step up to 10C. These results identify hydrothermally preorganized iron–carbon precursors as an effective design principle for low-temperature biomass graphitization and high-rate lithium-ion storage.

Received 7th July 2026
Accepted 14th September 2026

DOI: 10.1039/d6se00774k

rsc.li/sustainable-energy

Introduction

Graphite has long attracted interest from both academic and industrial communities because of its exceptional thermal stability, electrical conductivity, chemical resistance, mechanical robustness, and machinability.[1] These combined properties underpin its broad use in scientific and industrial applications. Among them, graphite is particularly important as the dominant anode material for lithium-ion batteries (LIBs), which are central to portable electronics, electric vehicles (EVs), and large-scale energy storage systems (ESS).[2,3] Graphite remains the preferred anode because it offers a theoretical capacity of 372 mAh g^{-1}, a low operating potential of ~0.1 V *versus* Li/Li^+, high coulombic efficiency, and long cycle life.[4,5] As demand for advanced batteries continues to grow, establishing a more secure and sustainable graphite supply has become a critical materials challenge.

At present, both natural graphite (NG) and synthetic graphite (SG) are widely used as anode active materials. However, NG supply is vulnerable because mining capacity is geographically concentrated and expands slowly. SG therefore remains attractive because it offers higher purity, more consistent properties, and greater flexibility in precursor and microstructural design.[2] Conventional SG production, however, is highly energy intensive. Established graphitization technologies, such as the Acheson process, can require temperatures approaching 3000 °C, energy consumption of 5.5–12 MWh per ton of graphite, and batch production cycles of 13–16 days.[6,7] Large thermal losses further reduce energy efficiency and increase cost.[7] Even soft-carbon precursors such as petroleum coke or coal tar pitch often require severe conditions to achieve high graphitic ordering. These conditions also favor centralized infrastructure, which is not always well-suited to biomass feedstocks that are geographically distributed, heterogeneous, and often handled in a wet state. For such feedstocks, practical implementation

[a]*A Research Center of Supercritical Fluid Technology, Graduate School of Engineering, Tohoku University, 6-6-11, Aoba, Aza, Aramaki, Aoba-ku, Sendai, Miyagi 980-8579, Japan*

[b]*Center for Basic Research on Materials, National Institute for Materials Science, 3-13 Sakura, Tsukuba, Ibaraki 305-0003, Japan*

[c]*Graduate School of Advanced Engineering, Tokyo University of Science, 6-3-1, Niijuku, Katsushika, Tokyo, 125-8585, Japan*

[d]*Institute of Pure and Applied Sciences, Department of Physics, University of Tsukuba, 1-1-1 Tennodai, Tsukuba, Ibaraki, 305-8571, Japan*

[e]*Tsukuba Research Center for Energy Materials Science (TREMS), University of Tsukuba, 1-1-1 Tennodai, Tsukuba, Ibaraki, 305-8571, Japan*

[f]*Frontier Research Institute for Interdisciplinary Sciences, Tohoku University, 6-3 Aoba, Aza, Aramaki, Aoba-ku, Sendai, Miyagi 980-8578, Japan. E-mail: nakayasu@tohoku.ac.jp*

benefits from process configurations that minimize pre-processing requirements, reduce the need for dedicated drying capacity, and remain compatible with flexible or decentralized operation. Lower-temperature and shorter-duration graphitization routes are therefore attractive not only for reducing thermal demand but also for enabling more adaptable biomass-to-carbon processing in line with broader sustainability and net-zero goals.[8]

Among the proposed alternatives, catalytic graphitization has emerged as a promising strategy because it can induce graphitic ordering at substantially lower temperatures than conventional non-catalytic processes.[9] Iron is especially attractive owing to its low cost, abundance, and strong catalytic activity. In Fe-catalyzed graphitization, disordered carbon dissolves into iron-containing particles at elevated temperature and precipitates as ordered graphitic carbon after saturation, following a dissolution–precipitation mechanism.[10–12] For lignocellulosic precursors, however, the extent of graphitization depends strongly on the contact between catalytic species and the carbon matrix. Uniform dispersion of Fe within the precursor is therefore essential for producing highly crystalline graphite at reduced temperature.[13]

This makes precursor engineering particularly important. Liquid-phase impregnation with aqueous $Fe(NO_3)_3$ is a practical route to introduce Fe species into biomass before heat treatment.[14] Oxygen-containing functional groups in wood can coordinate Fe during impregnation, improving catalyst distribution within the lignocellulosic framework.[15,16] Upon heating under an inert atmosphere, these precursor species are converted into catalytically active iron-containing particles that mediate the transformation of amorphous carbon into graphitic domains.[11,12] In this context, hydrothermal carbonization (HTC) provides an attractive platform for precursor design and conditioning. Because HTC uses water as the reaction medium, it can directly process wet biomass without energy-intensive drying and convert lignocellulosic feedstocks into carbonaceous intermediates under relatively mild conditions.[12,17–21] Moreover, when combined with the introduction of aqueous Fe, HTC can facilitate the incorporation and redistribution of metal species within the precursor, thereby creating favorable conditions for subsequent catalytic graphitization. These features are particularly advantageous for distributed biomass resources, for which simplified front-end handling and tolerance to variable moisture content are important for practical implementation.[13]

Previous studies have demonstrated that biomass-derived graphite can be prepared *via* catalyst-assisted routes at lower temperatures than those used in traditional graphitization. For example, lignocellulose-derived carbon has been converted into artificial graphite at 1500 °C with reversible capacities up to 340 mAh g^{-1},[22] while hardwood biochar has been transformed into high-quality bio-graphite at 1200 °C using Fe catalysts, pre-heating, and slow cooling.[23] Other catalyst-assisted systems based on saccharides likewise confirm the feasibility of producing highly crystalline graphite and promising LIB anodes from renewable precursors.[24] Nevertheless, many reported routes still rely on annealing at ~1200–1500 °C together with tightly controlled thermal profiles, which, although industrially accessible, increase thermal losses at these high temperatures, reduce design margins for furnace linings and heating elements, and make temperature uniformity across large batches more difficult to maintain, thereby limiting throughput and practical scalability.[24–26]

To address these scalability challenges using a widely available regional feedstock, Japanese cedarwood (*Cryptomeria japonica*) was selected as the biomass precursor because it is a major and widely distributed plantation resource in Japan. Japanese Forestry Agency data indicate that planted forests cover approximately 10.09 million hectares and that Japanese cedar and cypress together account for approximately 70% of Japan's planted-forest area; many postwar Japanese cedar plantations have also reached an age suitable for harvesting and utilization.[27] Japanese cedar is a representative lignocellulosic material comprising cellulose, hemicellulose, and lignin, and its cell-wall organization varies between earlywood and latewood.[28,29] Previous studies of Japanese cedar and related Japanese conifer wood have shown that iron impregnation can modify char yield, surface area, and carbon structure during pyrolysis.[30,31] These characteristics make Japanese cedar a relevant and locally available model precursor for investigating the coupling of biomass architecture, iron chemistry, and catalytic graphitization. The selection of Japanese cedar does not, however, imply that the proposed process is limited to this species or that it is universally superior to other lignocellulosic feedstocks.

The central challenge is therefore not only to lower the graphitization temperature, but also to design a biomass-derived precursor in which catalytic iron species and reactive carbon are positioned at short length scales before high-temperature treatment. We address this challenge by using a short hydrothermal carbonization step as a precursor-architecture tool. In the present process, Fe-impregnated Japanese cedarwood (CJ) is converted within 15 min into an iron–carbon hydrochar containing reducible mixed iron oxide domains, including Fe_3O_4. These domains are not regarded as the final active catalyst themselves; rather, they provide a spatially preorganized reservoir of iron that is converted during 1000 °C annealing into Fe/Fe_3C catalytic interfaces. This precursor architecture promotes the formation of highly ordered graphite, including local single-crystal-like graphitic domains. This highly crystalline development is corroborated by recent X-ray diffraction and structural analyses of cellulose-derived biocarbons, which confirm that metal catalysts efficiently drive the phase transformation of amorphous and turbostratic carbon into medium to long-range ordered graphitic structures.[32] The resulting material exhibits reproducible high-rate lithiation behavior as a lithium-ion battery anode. The study thus links hydrothermal precursor chemistry, low-temperature catalytic graphitization, and electrochemical rate performance in a single biomass-to-graphite strategy.

Results and discussion

The process begins with a primary HTC step at 250 °C for different reaction times, enabling Fe incorporation within the

 This journal is © The Royal Society of Chemistry 2026

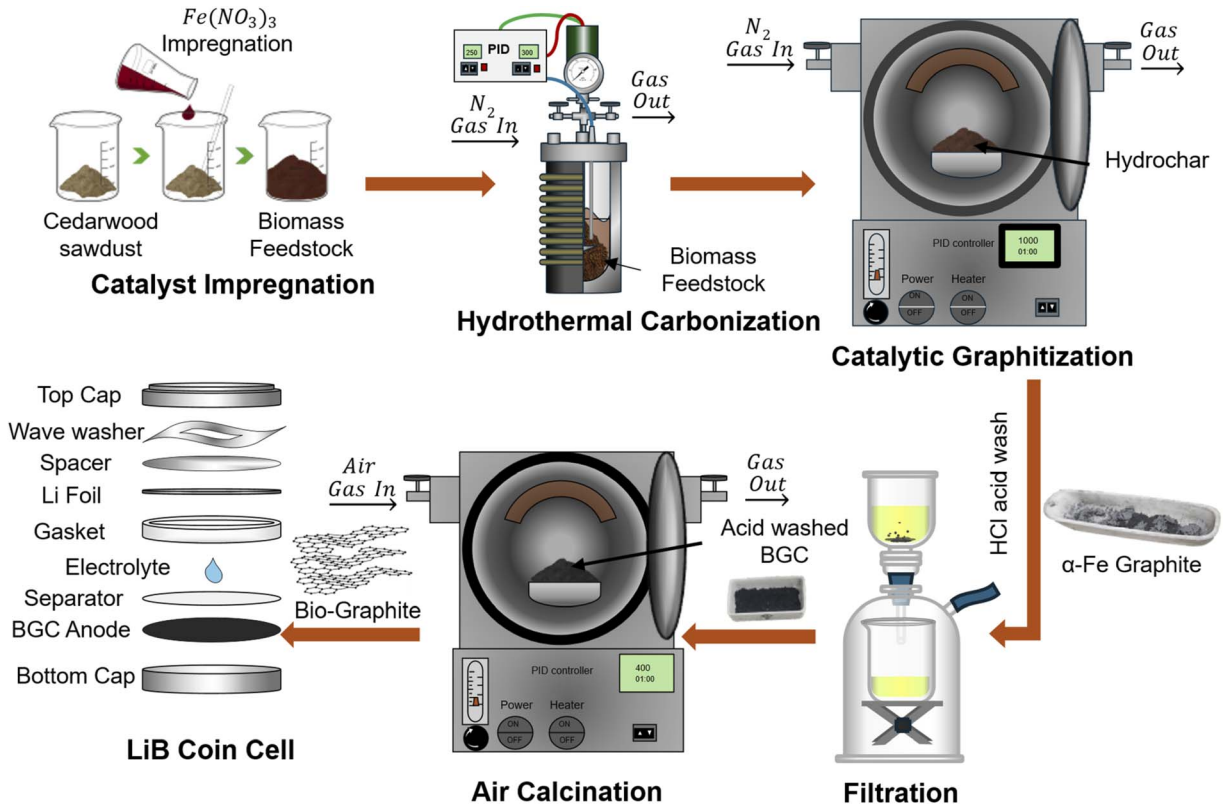


Fig. 1 Schematic representation of the experimental procedure carried out in this study.

wood-derived structure. Subsequent graphitization at 1000 °C under N_2 flow promotes the formation of graphitic domains. A final air calcination step at 400 °C selectively removes residual defect-rich or amorphous carbon, as illustrated in Fig. 1.

Rapid generation of a hydrothermally preorganized iron–carbon precursor

The X-ray diffraction (XRD) patterns of samples synthesized at 250 °C for durations ranging from 15 min to 4 h show principal reflections consistent with a spinel-like Fe_3O_4 phase. The diffraction peaks align well with the characteristic inverse spinel structure of magnetite, with the most intense reflection at ~35.4° corresponding to the (311) plane, along with additional peaks indexed to the (220), (400), (511), and (440) planes as shown in Fig. 2a. These peak positions and relative intensities are consistent with previously reported hydrothermal synthesis of magnetite-based carbon composites at slightly lower temperatures (230 °C). This similarity suggests that magnetite formation is favored under the present hydrothermal conditions.[33]

The XRD patterns show minimal variation across different residence times, indicating that magnetite crystallization occurs rapidly under these conditions and reaches a structural plateau within 15 min. While the phase appears stable within the investigated time window, magnetite is known to be susceptible to oxidation under hydrothermal conditions. For example, partial transformation to hematite (Fe_2O_3) has been reported at elevated temperatures. In the present data, no unambiguous reflections attributable solely to α-Fe_2O_3 were resolved by XRD. This may reflect peak overlap, limited crystallite size, or insufficient long-range ordering and does not exclude a substantial hematite-like contribution. As discussed below, Fe K-edge XANES linear-combination fitting indicates mixed Fe_3O_4- and α-Fe_2O_3-like environments.[33]

Importantly, the formation of Fe_3O_4 at this early stage plays a critical role in the subsequent graphitization behavior.[34] Although Fe_3O_4 itself is not the most active catalytic phase, it serves as a precursor to catalytically active iron species during high-temperature treatment. Upon carbonization at 1000 °C, Fe_3O_4 can undergo reduction and restructuring to form transient metallic iron or iron carbide species, which facilitate the reorganization of disordered carbon into ordered sp^2-bonded graphitic domains.[35–37]

This catalytic transformation is reflected in the thermogravimetric behavior. Thermogravimetric analysis (TGA) of the hydrochar precursors under an air atmosphere shows clear residence-time-dependent decomposition, where the 15 min sample exhibits significant weight loss at 300–400 °C, likely due to the presence of reactive intermediates and residual volatile species from incomplete biomass decomposition, as shown in Fig. 2b.[38] Longer residence times result in more stabilized hydrochar with reduced low-temperature decomposition. After Fe-catalyzed carbonization at 1000 °C, all bio-graphite (BGC) samples exhibit nearly identical oxidative TGA profiles, characterized by a sharp, single-stage combustion peak between

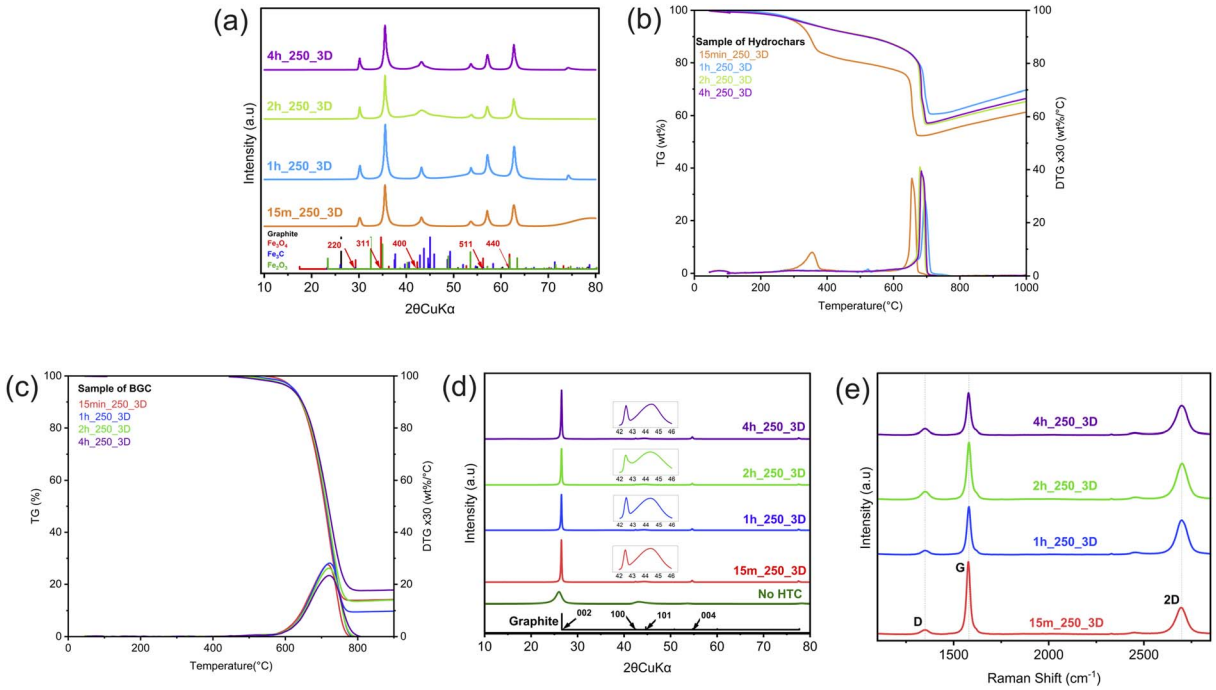


Fig. 2 XRD pattern of (a) hydrochar synthesized at 250 °C with varying residence time. Thermogravimetric (TG/DTG) analysis of (b) hydrochar and (c) BGC revealing progressive thermal stabilization, (d) XRD pattern and (e) Raman spectra of bio-graphitic carbon synthesized at 250 °C with varying residence time followed by 1000 °C graphitization.

~650 and 720 °C. This behavior is consistent with the combustion of ordered graphitic carbon structures formed through catalytic restructuring, as shown in Fig. 2c.[26]

The convergence of these oxidation profiles indicates the formation of a structurally uniform and thermally stable graphitic carbon matrix, irrespective of the initial differences in hydrochar composition. This transformation is enabled by the catalytic activity derived from Fe_3O_4, which reduces the influence of precursor-dependent heterogeneity during high-temperature treatment. The final plateau observed near 800 °C corresponds to the inorganic mineral ash content inherent to the original biomass feedstock, which remains consistent across all samples after complete combustion.[25,38] Consequently, even a short HTC residence time of 15 min is sufficient to produce a precursor capable of converting into high-quality graphitic carbon, highlighting the efficiency of the process.

Residence-time control of low-temperature graphitic ordering

Since this process depends strongly on the formation and activity of Fe species, hydrothermal residence time plays a critical role in determining the extent of graphitization. Therefore, the influence of hydrothermal residence time on graphitization was evaluated by XRD and Raman spectroscopy (Fig. 2d and e). Crystallite sizes were estimated from XRD data using the Scherrer equation. At the same time, Raman spectroscopy provided complementary information on defect density and graphitic domain development, derived from integrated peak areas (see SI for details). The structural parameters of each sample are summarized in Table 1.

To elucidate the role of the hydrothermal precursor architecture, a control sample was prepared by directly calcining Japanese cedarwood impregnated with aqueous $Fe(NO_3)_3$ at 1000 °C without the hydrothermal carbonization step (denoted as No HTC). The XRD pattern of the No HTC sample exhibits only a broad, low-intensity feature near 26°, which is characteristic of highly amorphous carbon with negligible layer stacking. This indicates that the hydrothermal pre-treatment is essential to closely embed and activate the precursor iron species within the matrix to initiate subsequent graphitic ordering. Notably, implementing a short HTC duration of only 15 min already produces a sharp, highly discernible (002) reflection. This rapid structural evolution yields a well-ordered domain with a crystal height L_c of approximately 46 nm, a lateral crystallite size L_a of approximately 69 nm, and an interlayer spacing (d_{002}) of 0.3369 nm, demonstrating that efficient catalytic graphitic stacking can be successfully activated even with minimal hydrothermal residence times.

Increasing the residence time to 1 h further enhances graphitic ordering, yielding the sharpest and most intense (002) peak ($L_c \approx 49$ nm, $L_a \approx 68$ nm, and $d_{002} \approx 0.3368$ nm), indicating optimal crystallite growth. However, extending the treatment to 2 h and 4 h leads to structural deterioration, as evidenced by peak broadening, reduced intensity, and decreased crystallite sizes (L_c: 44 → 35 nm; L_a: 67 → 49 nm). This degradation is attributed to structural collapse, excessive carbon consumption, and possible deactivation or agglomeration of Fe catalytic sites under prolonged hydrothermal conditions.

Raman spectra for all samples show characteristic D (~1350 cm^{-1}), G (~1580 cm^{-1}), and 2D (~2700 cm^{-1}) bands,

 This journal is © The Royal Society of Chemistry 2026

Table 1 Quantitative evaluation of crystallinity and disorder in bio-graphitic carbon *via* XRD and Raman spectroscopy

	XRD data (Scherrer equation)				Raman spectroscopy data (Tuinstra–Koenig relation)	
Sample name	FWHM (°)	Crystallite thickness, L_c (nm)	Lateral crystallite size, L_a, XRD (nm)	Interlayer spacing, d_{002} (nm)	I_D/I_G	Raman-derived lateral crystallite size, L_a (nm)
15 m_250_3D	0.1799	45.98	69.14	0.3369	0.18	107.59
1 h_250_3D	0.1699	48.69	67.8	0.3368	0.14	133.77
2 h_250_3D	0.1860	44.48	66.64	0.3366	0.23	82.88
4 h_250_3D	0.2376	34.82	48.74	0.336	0.27	71.65
MCMB	0.1411	58.62	124.63	0.337	0.17	114.58
Artificial graphite (coco peat)	0.3227	25.63	65.92	0.3377	0.44	43.51

confirming the formation of graphitic carbon. Notably, even the 15 min sample already exhibits a clear 2D band, indicating that early-stage graphitic stacking is consistent with XRD results. The 2D band is widely recognized as a sensitive probe of graphitic stacking order, capable of distinguishing turbostratic carbon from well-ordered graphite through its shape and evolution.[39]

Quantitatively, the (I_D/I_G) ratio decreases from 0.18 for the 15 min sample to 0.14 for the 1 h sample, accompanied by an increase in Raman-derived L_a from ~108 to ~134 nm, indicating reduced defect density and growth of graphitic domains. In contrast, longer residence times (2–4 h) result in increased I_D/I_G (0.23–0.27) and decreased Raman-derived L_a (~83–72 nm), reflecting increased disorder. These trends are consistent with XRD patterns and confirm that excessive HTC leads to structural degradation. These results demonstrate that short HTC durations (15 min–1 h) are sufficient to achieve substantial graphitic ordering ($L_c \approx$ 46–49 nm, $d_{002} \approx$ 0.3368–0.3369 nm) while avoiding degradation at longer times. From both structural and process perspectives, short-duration HTC provides a short-residence-time route for producing highly ordered biomass-derived graphitic carbon under the conditions investigated.

The persistence of the D band indicates that defects are inherent to biomass-derived carbon systems, although their concentration is minimized at the optimal residence time of 1 h. These results are consistent with previous reports showing that excessive hydrothermal treatment can lead to structural degradation, highlighting the importance of optimizing residence time.[40]

Thus, the 1 h condition gives the highest crystallinity, whereas the 15 min condition provides a process-relevant balance between short processing time and high graphitic ordering.

How precursor architecture promotes graphitization at 1000 °C

Iron-catalyzed graphitization of biomass is generally described as a high-temperature process in which iron precursors are transformed during pyrolysis into catalytically active Fe and/or Fe_3C particles that promote carbon ordering through dissolution–reprecipitation and carbide-mediated pathways. For example, $Fe(NO_3)_3$-impregnated lignocellulosic biomass has been reported to yield graphitic carbon *via* thermal decomposition of the iron salt, followed by carbothermal reduction and *in situ* Fe_3C formation.[41] More generally, iron-catalyzed graphitization is considered to proceed through the formation of iron oxide nanoparticles and their subsequent conversion into Fe and/or Fe_3C during high-temperature treatment.[42–44] In these conventional systems, however, the catalytically active phases are mainly generated during pyrolysis itself.

Building on our previous observation that the crystallite height (L_c) of graphitic carbon increases with Fe_3O_4 crystallite size in hydrothermally prepared precursors, hydrothermally formed Fe_3O_4 is regarded as a spatially preorganized and chemically pre-reduced precursor embedded within the hydrochar matrix.[34] Under hydrothermal conditions, oxygen-containing functional groups derived from biomass intermediates can coordinate Fe species, while reducing organic compounds generated from polysaccharide and lignin degradation partially reduce Fe(III) to Fe(II), thereby creating a mixed Fe(II)/Fe(III) redox environment favorable for magnetite formation. This process can be schematically represented as follows:

$$Fe^{3+} + xH_2O \rightleftharpoons Fe(OH)_{x^{3-x}} + xH^+$$

The hydrolyzed iron species then bind to the oxygen-containing functional groups (X = O or COO) on the biomass surface:

$$(3-x)\text{Biomass} - XH + [Fe(OH)_x]^{(3-x)+} \rightarrow [Fe(\text{biomass} - X)_{3-x}(OH)_x] + (3-x)H^+$$

$$R\text{–}CHO + 2Fe^{3+} + H_2O \rightarrow R\text{–}COOH + 2Fe^{2+} + 2H^+$$

followed by magnetite crystallization:

$$Fe^{2+} + 2Fe^{3+} + 4H_2O \rightarrow Fe_3O_4 + 8H^+$$

or, under local hydrolysis/precipitation conditions,

$$Fe^{2+} + 2Fe^{3+} + 8OH^- \rightarrow Fe_3O_4 + 4H_2O$$

Such behavior is consistent with previous reports on hydrothermally prepared Fe_3O_4/carbon composites, where biomass-

derived organics act simultaneously as reducing agents and carbon sources, stabilizing Fe_3O_4 particles.[45–47] Importantly, Fe_2O_3 could also serve as a reducible iron oxide precursor because hematite can be converted into metallic Fe through the sequential reduction pathway

$$\alpha\text{-}Fe_2O_3 \rightarrow Fe_3O_4 \rightarrow FeO \rightarrow Fe$$

under carbothermal conditions.[48,49] However, in the present hydrothermal system, Fe_3O_4 is particularly significant because its formation before annealing indicates that partial reduction of Fe(III) to Fe(II) and crystallization of a mixed-valence iron oxide have already occurred within the hydrochar matrix. This assignment is supported not only by XRD analysis but also by Fe K-edge XAFS characterization of the hydrothermally treated samples. As shown in the XANES region (Fig. 3a), the absorption edge positions of all experimental samples (15 min to 4 h) exhibit a prominent blue-shift relative to the metallic Fe-foil and FeO ref. 50. Instead, the edges align closely with the higher valence Fe_3O_4 and α-Fe_2O_3 standards, indicating that metallic Fe^0 and FeO are not dominant detectable components under the present measurement conditions; their complete absence cannot be established.[51] The identical pre-edge features, the same absorption energies, and the overlapping main peak profiles (Fig. 3a) qualitatively point to similar mixed-oxide environments across the investigated residence times. To estimate the relative contributions of the reference phases, linear combination fitting (LCF) of the XANES spectra was conducted (Table S4). At the onset of the reaction (15 min), the sample comprises 46% Fe_3O_4 and 54% α-Fe_2O_3. Extending the reaction time to 1 h results in a minor oxidation event, marginally increasing the α-Fe_2O_3 content to 60%. For the 2 h and 4 h samples, the fitted phase fractions remain approximately constant at 44% Fe_3O_4 and 56% α-Fe_2O_3.[52]

The limited time-dependent structural change is further supported by the Fourier-transformed (FT) k^3-weighted EXAFS spectra (Fig. 3b). All experimental samples display nearly identical radial distribution functions, indicating similar local Fe coordination environments across the investigated residence times. The first peak located at approximately 1.4 Å (uncorrected for phase shift) corresponds to the first-shell Fe–O scattering.[50] The second intense feature at roughly 2.7 Å is attributed to the Fe–Fe scattering shells associated with mixed Fe_3O_4- and α-Fe_2O_3-like environments. No distinct metallic Fe–Fe scattering feature comparable to that of the Fe foil reference at approximately 2.2 Å was detected within the sensitivity of the present measurements. Together, the XANES, LCF, and EXAFS results show no substantial time-dependent structural change after 15 min at 250 °C within the resolution of the present measurements.[51]

Upon subsequent annealing at 1000 °C under N_2, the embedded Fe_3O_4 can be carbothermally reduced by the surrounding carbon to form catalytically active Fe and/or Fe_3C species:

$$Fe_3O_4 + C \rightarrow 3FeO + CO$$

$$FeO + C \rightarrow Fe + CO$$

or, overall,

$$Fe_3O_4 + 4C \rightarrow 3Fe + 4CO$$

followed by phase-dependent iron carbide formation and decomposition:

$$3Fe + C \rightleftharpoons Fe_3C$$

$$Fe_3C \rightarrow 3Fe + C(\text{graphitic})$$

The resulting Fe/Fe_3C particles can subsequently catalyze the rearrangement of amorphous carbon into ordered graphitic domains through a dissolution–reprecipitation process:

$$C_{\text{amorphous}} \rightarrow C_{\text{dissolved}\in \text{Fe}} \rightarrow C_{\text{graphitic}}$$

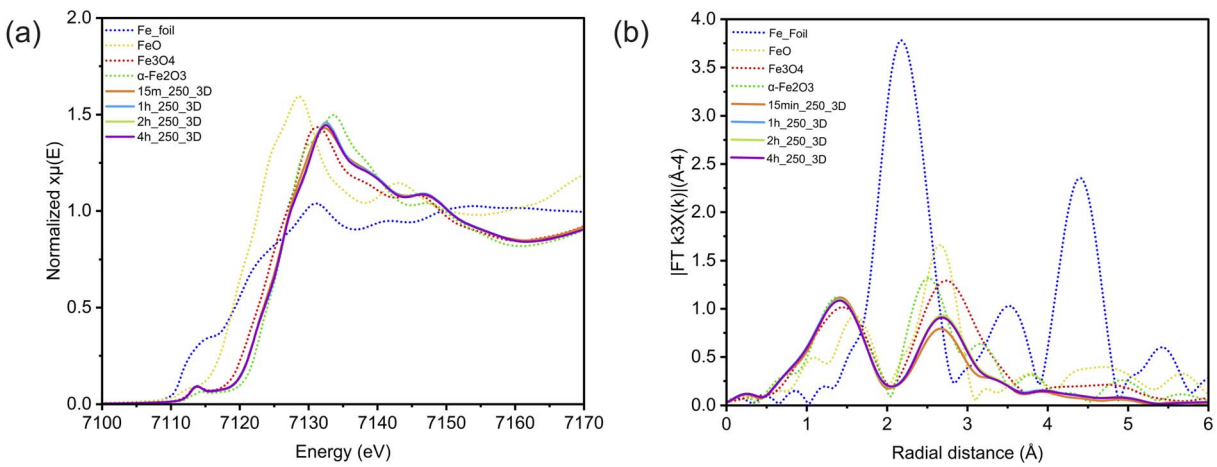


Fig. 3 Fe K-edge X-ray absorption spectra of the experimental samples treated at 250 °C over various reaction times compared to standard reference materials: (a) normalized XANES spectra with the corresponding pre-edge region shown in the inset, and (b) Fourier-transformed (FT) k^3-weighted EXAFS spectra.

 This journal is © The Royal Society of Chemistry 2026

Therefore, the high crystallinity of the final graphite-like carbon can be attributed to two sequential and interconnected processes: first, the hydrothermal formation of crystalline Fe_3O_4 within the hydrochar matrix, and second, the carbothermal conversion of this embedded Fe_3O_4 into active Fe/Fe_3C graphitization catalysts during annealing. The hydrothermal step should be interpreted as a precursor-architecture process. Scanning electron microscopy (SEM) and energy-dispersive X-ray spectroscopy (EDS) were used to evaluate the morphology and elemental composition of the hydrochar (15 min to 4 h), as shown in Fig. S3–S7 (SI). The SEM micrographs reveal a highly irregular, rugged, and porous surface microstructure inherited from the lignocellulosic cellular walls of the cedar wood biomass. EDS elemental mapping shows that Fe signals are broadly distributed across the examined hydrochar regions, consistent with widespread incorporation of the iron precursor during the hydrothermal step. The phase identity of the Fe-containing species is assigned from the combined XRD and XAFS results rather than from EDS alone. XRD confirms the rapid formation of crystalline iron oxide domains in the hydrochar, while Fe K-edge XAFS indicates that the iron phase is better described as a mixed iron oxide state rather than purely metallic iron or a single Fe_3O_4 phase. Thus, the mechanistic importance of the hydrothermal product lies not in Fe_3O_4 as an isolated active catalyst, but in the formation of reducible iron oxide domains intimately embedded within a reactive wood-derived carbon matrix.

Selective structural refinement by acid washing and mild air oxidation

After catalytic graphitization under a nitrogen atmosphere and subsequent acid washing, a certain amount of defect-rich or amorphous carbon remained. Therefore, air calcination was conducted at 400 °C for 1 h to selectively remove residual defect-rich or amorphous carbon and enhance the relative graphitic ordering of the carbon material. X-ray diffraction (XRD) was used to track the structural evolution and crystallinity enhancement of the 15 m_250_3D carbon sample, as shown in Fig. 4a, from hydrochar to final air-treated graphite, compared against reference graphite. The hydrochar displayed a broad carbon-related feature around 26.5°, characteristic of low graphitic ordering, along with peaks corresponding to Fe_3O_4, indicating the formation of iron oxide species during HTC. In the "before HCl" sample, only α-Fe was detected near 45°, confirming the partial reduction of iron species, although complete removal had not yet occurred due to the absence of acid washing. After HCl washing, the (002) reflection became more prominent, while no diffraction peaks attributable to crystalline Fe-containing phases were detected within the detection limit of XRD. This observation is consistent with the removal of XRD-detectable crystalline and exposed Fe-containing species but does not establish complete Fe removal. Subsequent air oxidation at 400 °C for 1 h intensified the graphitic reflections and decreased the Raman I_D/I_G ratio, indicating selective removal of defect-rich or amorphous carbon. Because the XRD-derived L_c changed only slightly after air calcination, this treatment is interpreted as a structural refinement step that increases the relative fraction of ordered graphitic domains rather than inducing substantial additional crystal growth. These features closely resemble those of the reference artificial graphite.

The progressive sharpening of the (002) peak, together with the absence of XRD-detectable crystalline Fe-containing phases after acid washing, supports the structural evolution of the acid-washed product toward highly ordered graphitic carbon. EDS analysis of selected regions showed only a weak Fe signal in BGC and post-air BGC (Table S6); however, because EDS is local and semi-quantitative, trace, amorphous, or highly dispersed residual Fe cannot be excluded without bulk elemental quantification, and its possible contribution to the observed properties cannot be completely ruled out. The (100) and (101) reflections further provide insight into the in-plane structural order. Although commercial MCMB shows sharp and intense diffraction peaks indicative of a highly ordered graphitic structure, artificial graphite exhibits comparatively broader and less defined reflections. Interestingly, both the BGC (before air calcination) and air-treated BGC samples present significantly broadened features, characteristic of turbostratic or nanocrystalline carbon domains. Importantly, air calcination does not markedly influence the position or profile of the in-plane reflections, indicating that the underlying crystalline

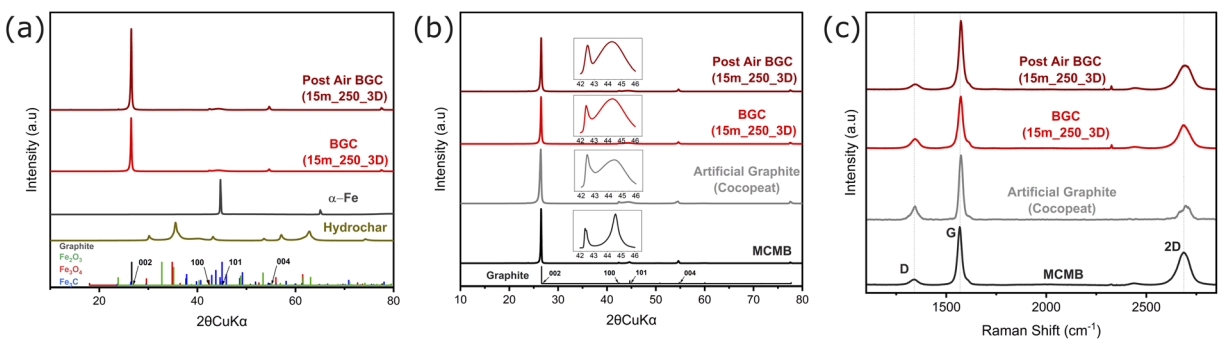


Fig. 4 XRD patterns (a) show phase evolution from hydrochar to Fe-assisted bio-graphitic carbon before and after air calcination, (b) comparison of (002) peak profiles highlighting crystallinity differences between BGC, artificial graphite, and MCMB (c) Raman spectra illustrating defect-to-graphitic ordering transition in BGC compared with commercial graphitic carbons.

Table 2 Raman- and XRD-derived structural parameters of 15 m_250_3D carbon before and after air calcination

Sample	I_D/I_G	L_a (nm)	L_c (nm)
Before calcination	0.18	107.59	45.98
After calcination	0.14	134.52	44.86
Artificial graphite (coco peat)	0.44	43.51	25.63
MCMB	0.17	114.58	58.62

framework remains intact, while predominantly removing surface-associated disorder as shown in Fig. 4b. Notably, a slight decrease in the crystallite height (L_c) from 45.98 nm to 44.86 nm was observed after air calcination, which may be attributed to the mild oxidation-induced removal of amorphous carbon, resulting in a marginal reduction in stacking height without compromising the overall graphitic framework as shown in Table 2.

Raman analysis further confirms this structural refinement. The N_2-carbonized 15 m_250_3D sample exhibits an I_D/I_G ratio of 0.18, corresponding to a Raman-derived in-plane crystallite size (L_a) of 107.6 nm. After air calcination, the I_D/I_G ratio decreases to 0.14, accompanied by an increase in L_a to 134.5 nm, indicating a clear reduction in defect density and an increased relative fraction of ordered graphitic domains. Interestingly, the air-treated sample achieves a Raman-derived L_a comparable to that of the optimized 1 h sample (see Table S3), suggesting that mild oxidative treatment can partly compensate for shorter hydrothermal residence times by removing defect-rich carbon. This behavior is consistent with established studies showing that selective oxidation removes disordered or amorphous carbon phases, thereby enhancing the relative proportion of graphitic domains and improving overall crystallinity. Reductions in I_D/I_G ratios following oxidative treatment have been widely reported as evidence of microstructural refinement in hybrid amorphous/graphitic carbon systems.[53,54]

Qualitatively, the Raman spectra show a suppression of the D-band intensity and a more symmetric and intense 2D band after air treatment, consistent with a reduced relative contribution from defect-rich carbon and an increased contribution from graphitic domains. These observations are consistent with XRD results and further support the conclusion that air calcination acts as a structural refinement step. Controlled oxidation is known to preferentially target loosely bound, amorphous, or defect-rich carbon regions, particularly at the surface, thereby preferentially removing reactive surface-associated carbon without producing a substantial change in the XRD-derived stacking thickness, as shown in Fig. 4c.[55] However, the effectiveness of this approach depends critically on the severity of treatment, as excessive oxidation can lead to carbon loss and lattice etching.[56] In this study, controlled air oxidation provides a practical structural-refinement step under the conditions examined, although direct TEM/HRTEM and XPS comparisons would be required to resolve local lattice and surface-chemical changes.

Comparative SEM images obtained before and after air treatment are shown in Fig. S8. After air treatment, the fine surface overlayer becomes less prominent and larger carbonaceous domains are more clearly exposed. These images provide complementary evidence of an accompanying morphological change. However, SEM does not directly resolve local lattice ordering or surface chemical states; therefore, it is not used as direct evidence of crystallization. The interpretation of the air treatment is limited to preferential removal of reactive or disordered carbon and the resulting relative enrichment of graphitic domains inferred from the combined XRD and Raman results.

Process-relevant short-time synthesis and preliminary scale-up

To evaluate the process's carbon retention efficiency, elemental analysis (CHNSO) was conducted on the CJ (Table 3).

The resulting carbon content was used to calculate the carbon yield of the biomass-derived graphitic carbon (BGC) obtained under the selected 15 min HTC and 1000 °C annealing conditions. The carbon yield was determined using the following equation:

$$\text{Carbon yield}\left(\frac{w}{w}\%\right) = \frac{\text{Mass of BGC}}{\text{Mass of SD} \times \text{Carbon content}} \times 100$$

Here, an assumed carbon fraction of 0.99 was used to provide an approximate estimate of carbon retention in the final graphitic carbon after acid washing and air oxidation.

The influence of residence time on both hydrochar and carbon yield was systematically assessed. A gradual decline was observed in both metrics as the residence time increased: mass yield decreased from 0.80% at 15 min to 0.74% at 4 hours, while carbon yield fell from 1.60% to 1.47% as shown in Fig. 5a. These modest reductions indicate that prolonged HTC promotes additional volatilization and decomposition of thermally sensitive constituents, resulting in lower solid recovery. This trend is well-supported by literature, which shows that increasing residence time enhances biomass degradation through hydrolysis and subsequent reactions, shifting product distribution toward bio-oil and gaseous phases rather than solid hydrochar. Reactions such as decarboxylation and dehydration, which occur rapidly at early stages but continue with extended treatment, contribute to progressive carbon loss and reduced solid yield. Consequently, shorter residence times appear more effective for retaining both total mass and carbon, highlighting their suitability for energy-efficient hydrochar production.[57]

Table 3 CHNSO elemental composition of CJ used as the biomass feedstock

	Elements				
Samples	C (%)	H (%)	N (%)	S (%)	O (%)
CJ	49.81	6.04	0.14	NIL	43.29

This journal is © The Royal Society of Chemistry 2026

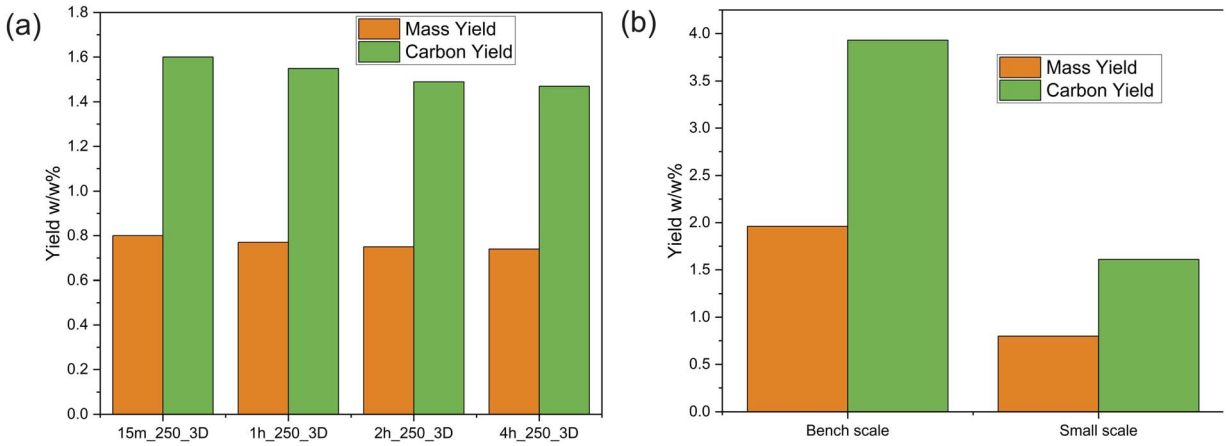


Fig. 5 Mass yield and carbon yield of BGC as a function of (a) HTC residence time and (b) comparison of bench-scale and small-scale synthesis.

This behavior is consistent with trends reported in previous studies. Ghanim *et al.* demonstrated that hydrochar yield generally decreases with increasing HTC severity, although fixed carbon content and energy density tend to improve under such conditions.[58] Similarly, Reza *et al.* observed reduced carbon recovery with increasing temperature and residence time, attributed to enhanced dissolution of organic and inorganic fractions into the process water.[59] More broadly, it is widely recognized that while temperature is the dominant parameter governing HTC severity, residence time remains a critical factor controlling the extent of feedstock decomposition and preservation of the carbon matrix.[57] The observations in the present study, therefore, reinforce that HTC severity, whether controlled through time or temperature, plays a decisive role in governing hydrochar yield and carbon retention.

To examine preliminary transferability beyond the original batch size, bench-scale experiments were conducted under the 15 min HTC condition using a reactor volume and biomass loading four times larger than those of the small-scale setup. The scaled 15 m_250_3D sample showed a substantial increase in both mass and carbon yield compared with the small-scale sample: mass yield more than doubled, from 0.80% to 1.96%, while carbon yield increased by approximately 2.5 times, from 1.60% to 3.93%, as shown in Fig. 5b. These results demonstrate that the process could be reproduced at a larger laboratory batch size under the tested conditions; however, they should not be interpreted as evidence of industrial scalability.

The higher yield observed in the bench-scale experiment may reflect differences in reactor geometry, heat-transfer history, liquid-to-solid contact, and material handling losses between the two scales. Accordingly, the difference in yield cannot be attributed solely to the fourfold increase in biomass loading or to the 15 min residence time. Because these factors can strongly affect HTC product recovery, further scale-up studies with controlled heat-transfer and mixing conditions are required to determine their relative contributions. It is well established that, although intrinsic reaction kinetics remain scale-independent, physical parameters such as heat transfer, mixing, and mass transport govern reactor performance and product selectivity during scale-up.[60,61] Poor control over these parameters can lead to temperature gradients and undesired side reactions, ultimately reducing yield, whereas improved transport conditions can help preserve the carbon matrix and enhance solid recovery.[62,63]

In contrast, the decreasing yields observed at longer residence times suggest that extended HTC promotes volatilization and thermal degradation, ultimately lowering the amount of recoverable carbon. Thus, the high recovery obtained with the 15 min condition under the present conditions is consistent with reduced structural degradation, whereas the additional increase observed in the larger-scale experiment may be associated with scale-dependent differences in heat transfer, mixing, liquid–solid contact, and recovery efficiency.

The results therefore support short-duration HTC as a favorable condition for bench-scale hydrochar production under the conditions investigated. Nevertheless, catalytic graphitization at industrially relevant scale will require additional assessment of catalyst distribution, catalyst residue retention, catalyst recovery and reuse, heat and mass transfer, temperature uniformity, energy consumption, reactor throughput, and process economics. The present 10–40 g comparison should consequently be regarded as a preliminary laboratory-scale scale-up assessment rather than a demonstration of commercial feasibility. Further experiments at progressively larger batch sizes or under continuous operation will be necessary to determine whether the observed yield and material-property trends are maintained when transport limitations and catalyst-management requirements become more significant.[60–63]

Local single-crystal-like graphitic domains in a polycrystalline sheet network

The SEM images of BGC (15 m_250_3D), shown in Fig. 6a, reveal a heterogeneous and highly aggregated morphology over the micrometer scale. At lower magnification, the carbon exhibits irregular aggregates containing larger lamellar and fibrous features together with finer fragmented structures. At higher

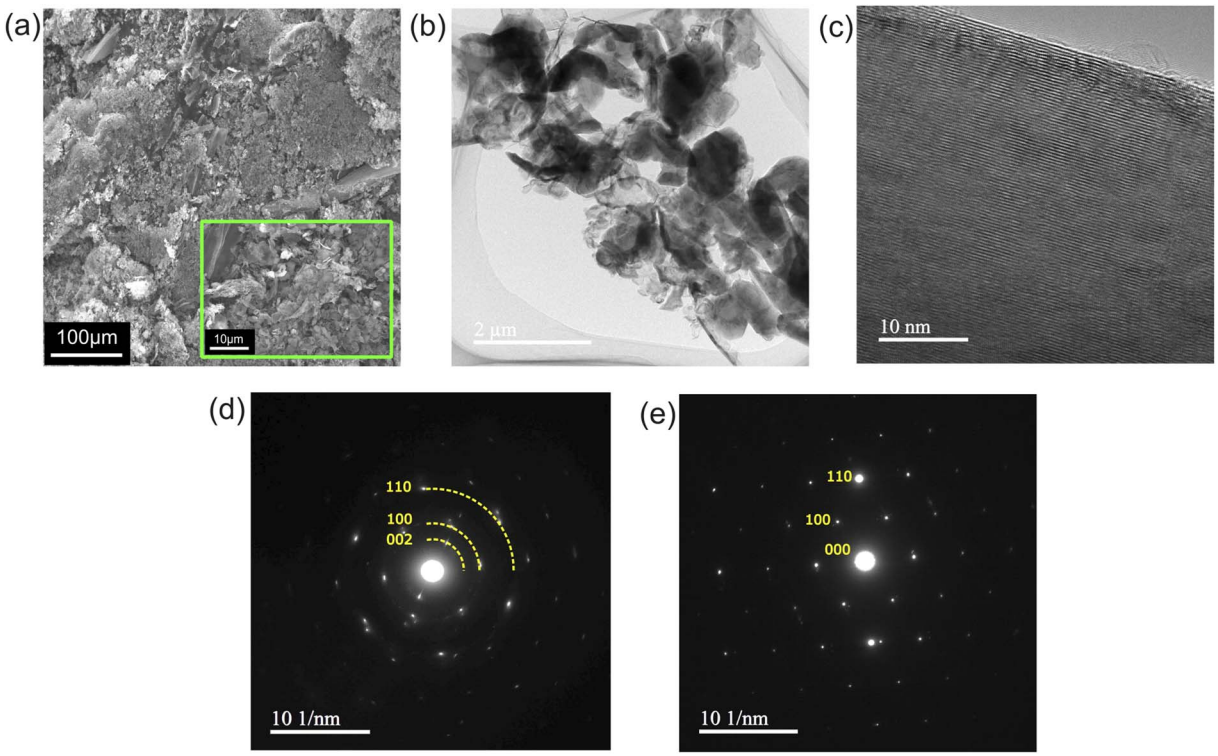


Fig. 6 Multiscale morphology and local graphitic ordering of BGC (15 m_250_3D): (a) SEM images obtained at low and high magnification; (b) TEM image showing crumpled sheet-like aggregates; (c) HRTEM image showing graphitic lattice fringes; (d) SAED pattern from a polycrystalline or textured graphitic region; and (e) SAED pattern showing discrete hexagonally arranged diffraction spots from a locally highly oriented graphitic region.

magnification, numerous wrinkled and flake-like carbon fragments are observed, suggesting substantial morphological reconstruction of the biomass-derived carbon during hydrothermal treatment and subsequent Fe-assisted graphitization. The coexistence of larger carbonaceous structures and finely divided sheet-like fragments indicates a hierarchical morphology with considerable structural heterogeneity. These SEM observations provide the microscale morphological context for the crumpled and sheet-like structures observed by TEM. At the nanoscale, the transmission electron microscopy (TEM) analysis, as shown in Fig. 6b, reveals crumpled, sheet-like carbon structures forming loosely packed aggregates, which are characteristic of biomass-derived carbon materials.[25,64] These irregular morphologies reflect the preservation of structural templates during carbonization and are commonly observed in hydrothermally and thermally treated biomass chars, where complex, multi-scale architectures are formed.[57,64] TEM images further indicate notable structural heterogeneity, with semi-transparent regions corresponding to thin, few-layer graphitic domains, while darker, opaque regions represent thicker, multilayer graphitic assemblies.[55,65] The observed wrinkling and folding originate from the reconstruction processes during biomass decomposition and subsequent catalytic graphitization.[56,65] Moreover, the interconnected and sheet-like morphology may facilitate electrolyte access and Li^+ transport, contributing to the observed rate capability.[57,66] This hierarchical structural organization, consisting of both ordered and disordered domains, confirms the effectiveness of the rapid Fe-assisted catalytic graphitization process in converting biomass into graphitic carbon.[55,65]

In Fig. 6c, high-resolution transmission electron microscopy (HRTEM) confirms that the final BGC contains extended parallel lattice fringes with an interlayer spacing of approximately 0.33–0.34 nm,[25,66,67] consistent with graphite (002) stacking.[56,65,66] In addition to polycrystalline ring-like SAED patterns, selected regions exhibit discrete diffraction spots arranged with hexagonal symmetry. These spots are assigned to in-plane graphite reflections and indicate local single-crystal-like graphitic domains viewed close to the [0001] zone axis.

The extended and continuous nature of these fringes indicates a high degree of graphitic stacking order, while slight distortions and curvature suggest the presence of defects or turbostratic stacking in certain regions.[34,55,68] These observations confirm the formation of graphitic carbon with a well-developed layered structure.[22]

In regions exhibiting polycrystalline characteristics, as shown in Fig. 6d, the selected area electron diffraction (SAED) pattern displays concentric diffraction rings with intensity modulation, indicating a polycrystalline graphitic structure with preferred orientation.[34,55,69] The innermost diffuse ring is indexed to the (002) plane, corresponding to interlayer stacking of graphene layers, while the outer rings are assigned to the (100) and (110) planes, reflecting in-plane crystallographic ordering.[43,70] The presence of discontinuous arcs rather than

 This journal is © The Royal Society of Chemistry 2026

continuous rings further confirms a textured polycrystalline nature with partially aligned graphitic domains.[55]

In contrast, other regions exhibit single-crystal-like diffraction features, as shown in Fig. 6e, where the SAED pattern shows well-defined, discrete diffraction spots arranged in a hexagonal symmetry, indicating locally highly ordered graphitic domains.[66,69] The central transmitted beam corresponds to the (000) reflection, while the surrounding diffraction spots are indexed to the (100) and (110) planes.[45,71] The absence of diffraction rings and the presence of sharp, periodically arranged spots indicate locally highly ordered graphitic domains with single-crystal-like diffraction features, consistent with a [0001] zone axis orientation where the electron beam is aligned parallel to the *c*-axis.[70,71]

Conventional biochar derived from direct biomass pyrolysis typically retains a rigid, blocky framework, resulting in a dense and monolithic morphology.[64] The Fe-assisted graphitization treatment substantially reconstructs the carbon architecture, resulting in a heterogeneous morphology comprising irregular aggregates, wrinkled/flake-like fragments, and locally sheet-like structures.[72] This transformation yields a hybrid morphology consisting of both few-layer graphene-like sheets and thicker multilayer graphitic domains, forming a hierarchical and interconnected structure.[25] Such structural evolution from a dense precursor to a sheet-like graphitic framework highlights the effectiveness of catalytic restructuring in reducing defect-rich carbon regions and enhancing graphitic ordering. The resulting material is structurally distinct from conventional biochar and provides a graphitic, sheet-like morphology suitable for lithium-ion storage.

High-rate discharge behavior of biomass-derived graphite without post-synthetic surface coating

The rate capability of the BGC electrode was first evaluated on the discharge/lithiation branch (Fig. 7a). In the graphite||Li half-cell configuration, discharge corresponds to Li^+ intercalation into graphite, whereas charge corresponds to Li^+ deintercalation. The lithiation capacity decreased progressively as the rate increased from 0.1C to 10C, consistent with increasing polarization and the reduced time available for Li^+ transport at high current.[73] Nevertheless, the capacity remained stable within each rate step, indicating reproducible operation of the BGC electrode under high-rate lithiation.

The charge/delithiation branch exhibited a greater capacity loss at high rates (Fig. S11). This difference should be interpreted as a protocol- and cell-dependent rate response rather than as evidence that Li^+ deintercalation is intrinsically more difficult than intercalation in graphite. At high current, electrolyte, solid-state, charge-transfer, and ohmic overpotentials can cause the voltage cutoff to be reached before Li^+ extraction is complete, particularly in a structurally heterogeneous porous electrode.[74] For biomass-derived catalytically graphitized carbon, variations in crystallinity, turbostratic disorder, pore structure, surface chemistry, and interfacial resistance may further broaden the distribution of Li^+ transport kinetics.[75] Because the lithiation and delithiation measurements were performed in separate cells, cell-to-cell differences may also contribute to the observed asymmetry. Accordingly, BGC is best described as exhibiting favorable high-rate lithiation performance, while its fast-rate delithiation remains limited under the present test conditions. Further optimization of electrode density, particle-size distribution, surface chemistry, and interfacial resistance is required to improve high-rate delithiation.

The electrochemical reversibility and early interfacial stabilization of the BGC electrode were further evaluated at 0.1C, as shown in Fig. 7b. The electrode exhibits an initial coulombic efficiency of approximately 93%, indicating limited irreversible Li consumption associated mainly with solid electrolyte interphase formation.[25,73,76] The coulombic efficiency increases during the initial cycles and reaches approximately 95% by the fifth cycle. Although this value still requires improvement for practical full-cell operation, the rapid stabilization suggests that the graphitic framework forms a relatively stable electrode–electrolyte interface without post-synthetic surface coating. The discharge/lithiation capacity also remains relatively stable during the initial cycles, indicating that the electrode maintains its accessible Li-storage capacity during early cycling. These five initial cycles are intended to evaluate the early electrochemical stabilization of the electrode and should not be interpreted as evidence of long-term cycling stability.

The cyclic voltammetry curves for the first three cycles are shown in Fig. 7c. The cathodic features correspond to lithiation, whereas the anodic features correspond to delithiation.[21,24] The close overlap of the second and third cycles indicates good early-cycle reversibility after initial SEI formation. This behavior is consistent with the formation of a stable graphitic host structure that can repeatedly accommodate Li insertion and extraction during the early cycles.

The galvanostatic charge–discharge profiles at 1C are shown in Fig. 7d. The first cycle includes irreversible capacity associated with SEI formation. In the second cycle, the lithiation and delithiation capacities are 341 and 317 mAh g^{-1}, respectively, corresponding to a coulombic efficiency of approximately 93% when calculated as the delithiation capacity divided by the lithiation capacity. By the third cycle, the delithiation capacity stabilizes at approximately 315 mAh g^{-1}, corresponding to about 85% of the theoretical capacity of graphite even at the accelerated 1C rate. The profiles exhibit clear low-voltage plateaus below 0.5 V *vs.* Li/Li^+, which are characteristic of staged Li^+ intercalation into graphitic layers.[22,24,67] The small cycle-to-cycle change in the voltage profiles further supports stable early-cycle reversibility of the BGC electrode.

The electrochemical performance of the BGC electrode is notable because the active material was used without any post-synthetic surface coating. In many graphite anode systems, carbonaceous coatings are introduced to passivate surface defects, suppress excessive electrolyte decomposition, and improve initial coulombic efficiency and cycling stability.[66] In contrast, the present BGC delivers high 1C lithiation/delithiation capacities and stable early-cycle behavior without such coating treatment. This indicates that the precursor-derived graphitic architecture, including low Raman disorder,

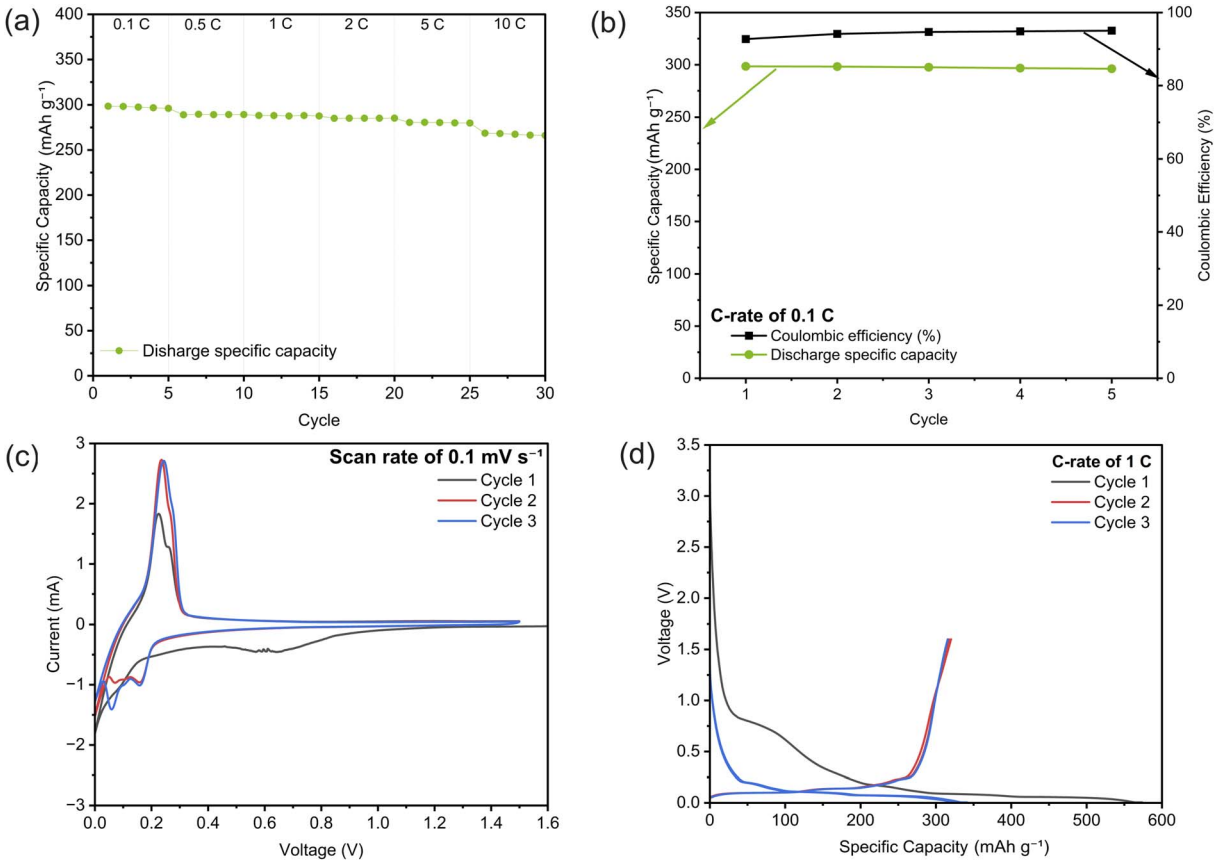


Fig. 7 Electrochemical performance of the BGC (15 m_250_3D) electrode: (a) lithiation rate capability over five cycles at each C-rate; (b) initial-cycle lithiation capacity and coulombic efficiency at 0.1C; (c) cyclic voltammograms recorded at 0.1 mV s^{-1}; and (d) galvanostatic lithiation/delithiation profiles at 1C.

graphite-like stacking, and local single-crystal-like graphitic domains, contributes to the intrinsic electrochemical quality of the material.

To place the electrochemical performance of the present BGC in context, Table 4 compares its synthesis conditions and lithium-storage behavior with representative biomass-derived graphitic anodes. Because graphite half-cells can show different lithiation/discharge and delithiation/charge responses at high C-rates, both branches are separated where the original reports provide sufficient information. When only reversible capacity is reported, the charge and discharge branches are not separated.

This comparison indicates that the present BGC should be positioned as a process-advantaged biomass-derived graphite rather than as a record-capacity material. Some recent biomass-derived graphites reach higher absolute capacities when processed at higher graphitization temperatures or when modified by dopants or lattice engineering. For example, pyrolysis-bio-oil-derived biographite can approach the theoretical capacity of graphite after graphitization at 1500 °C, and Nb-doped coffee-husk-derived biographite can deliver very high capacity through heteroatom/lattice engineering. In contrast, the present BGC, used without post-synthetic surface coating, delivers 341/317 mAh g^{-1} lithiation/delithiation capacities at 1C after only a 15 min HTC precursor-organization step and graphitization at 1000 °C. Thus, the advantage of the present material lies in the combination of low-temperature synthesis, short hydrothermal precursor organization, operation without post-synthetic surface coating, local single-crystal-like graphitic domains, and stable high-rate discharge/lithiation behavior.

From a processing perspective, eliminating post-synthetic coating reduces material complexity and avoids additional coating precursors and thermal treatments.[25,66] Therefore, the BGC developed in this study can be regarded as a process-advantaged graphite material that achieves promising lithium-ion storage performance through intrinsic structural quality rather than external surface modification. This result highlights the effectiveness of hydrothermal precursor architecture engineering for producing highly crystalline biomass-derived graphite suitable for high-rate discharge applications.

Because graphitization temperatures above 1000 °C were not systematically examined, 1000 °C should not be regarded as the fully optimized graphitization temperature. Rather, it is the lowest temperature evaluated in this study that produced graphite-like domains and promising electrochemical performance. Direct comparisons at 1200–1500 °C will be required to determine whether higher temperatures can further suppress the sloping capacity, improve graphitic ordering, and enhance lithiation/delithiation kinetics.

 This journal is © The Royal Society of Chemistry 2026

Table 4 Comparative overview of synthesis conditions and lithium-ion storage performance of biomass-derived graphitic anodes

Material/source	Feedstock and process	T_{max}	Discharge/lithiation benchmark	Charge/delithiation or reversible benchmark	Rate/cycling note
This work	Japanese cedarwood; $Fe(NO_3)_3$ impregnation; HTC 250 °C, 15 min; N_2 annealing; HCl washing; mild air oxidation; active material used without post-synthetic surface coating	1000 °C	341 mAh g^{-1} lithiation at 1C, 2nd cycle	317 mAh g^{-1} delithiation at 1C, 2nd cycle. Charge/delithiation at high C-rate; early CE *ca.* 93–95%	Discharge/lithiation rate branch remains comparatively stable up to 10C with 30 cycles
Dey *et al.*, *Energy Fuels* 2025 (ref. 77)	Pyrolysis bio-oil; low-temperature pretreatment 150–200 °C; Fe-catalyzed graphitization	1500 °C	Reported nearly theoretical specific capacity around 370 mAh g^{-1}	Separate charge/discharge values not available from abstract; ICE 90.03%	Minimal fading after 50 cycles in LIB half-cells
Gulas *et al.*, *ACS Omega* 2026 (ref. 78)	Industrial biomass-derived synthetic graphite; catalyst-free Acheson-type synthesis from wood/forestry residues	Industrial graphitization	Li^+ discharge at 0.1C: 331.0 mAh g^{-1} (BDSG B), 335.7 mAh g^{-1} (BDSG D)	First CE: 88.3% (BDSG B), 87.2% (BDSG D). 2C charging *vs.* 0.2C charging: 25.0% and 26.5%	3C discharging *vs.* 0.2C discharging: 59.7% and 68.6%
Dey *et al.*, *Green Chem.* 2024 (ref. 70)	Hardwood-derived pyrolysis oil; reduced Fe powder; acid washing	1500 °C	First/second discharge–charge profile reported; initial reversible capacity about 350 mAh g^{-1}	ICE 90.2%; CE stabilizes near 99% after initial cycles	Rate tested from 0.1C to 4C; capacity decreases with C-rate and recovers when returned to 0.1C
Jeong *et al.*, *J. Alloys Compd.* 2025 (ref. 22)	Lignocellulose + Fe catalyst; catalytic graphitization at 1500–2500 °C	1500–2500 °C	L-AG-2500 shows around 340 mAh g^{-1}; L-AG-1500 around 300 mAh g^{-1}	Not separated in abstract; described as reversible capacity	Stable over 100 cycles; high-rate capability up to 5C, but rate capability described as inferior and needing improvement
Wang *et al.*, *Sustainable Energy Fuels* 2025 (ref. 79)	Wheat straw, rice straw, corn stalks; K_2CO_3–Na_2CO_3 molten-salt electrolysis; silica removal assists graphitization	850 °C electrolysis	Graphite anode: 293 mAh g^{-1} at 0.1 A g^{-1}	Not separated in article landing page	Commercial graphite comparison: 287.8 mAh g^{-1} at 0.1 A g^{-1}
Thomas *et al.*, *MRS Energy & Sustainability* 2026 (ref. 80)	Fe-catalyzed cellulose/dextrin/lignin pyrolysis	1400 °C	Fe-catalyzed cellulose: second-cycle discharge capacity 296 mAh g^{-1}	Average reversible capacity 278 mAh g^{-1} over five cycles; ICE 77.2% for cellulose	C/8 half-cell protocol; full-cell cellulose case reported 304 mAh g^{-1} initial capacity and 71.6% retention after 70 cycles in the better cell
FlatChem 2025 coffee-ground bio-graphite[81]	Waste coffee grounds; Fe-catalyzed graphitization; C-AG *vs.* hard carbon	1500 °C	C-AG around 286 mAh g^{-1}	ICE 85.5%; charge/discharge split not available from abstract	Stable at various current densities
Borges *et al.*, *J. Power Sources* 2026 (ref. 82)	Nb-doped biographite from coffee husk biomass	Not directly comparable	Specific discharge capacity 375 mAh g^{-1} at 0.2C	Charge value not separated in abstract	High cycling stability; full LIB cell also assembled

Conclusions

This study demonstrates short-time hydrothermal carbonization as a precursor-architecture strategy for low-temperature graphitization of Fe-impregnated Japanese cedarwood. A 15 min HTC step at 250 °C forms an iron–carbon hydrochar containing reducible mixed iron oxide domains, including Fe_3O_4, embedded within a reactive carbon matrix. During annealing at 1000 °C, these domains serve as spatially preorganized iron reservoirs that are converted into Fe and/or Fe_3C catalytic phases, promoting graphitic layer growth. Subsequent acid washing was used to leach acid-soluble and exposed Fe-containing species, while mild air oxidation preferentially removed reactive or defect-rich carbon. No crystalline Fe-containing phases were detected by XRD after washing, although trace residual Fe cannot be excluded without bulk elemental quantification. The resulting biomass-derived graphite, used without post-synthetic surface coating, exhibits graphite-like stacking, low Raman disorder, and local single-crystal-like graphitic domains within an interconnected sheet network. As a lithium-ion battery anode, the material delivers 341/317 mAh g^{-1} lithiation/delithiation capacities at 1C and exhibits reproducible lithiation behavior within each rate step up to 10C, while high-rate delithiation remains limited under the present test conditions. Thus, the main advantage of the present BGC is not the highest absolute capacity among biomass-derived graphites, but the combination of short precursor organization, 1000 °C graphitization, operation without post-synthetic surface coating, local graphitic ordering, and high-rate discharge capability. The rate-limited charge/delithiation branch at high C-rates further identifies electrode densification, particle-size control, and interfacial optimization as key targets for future fast-charge operation.

Experimental

Materials and chemicals

Japanese cedarwood (*Cryptomeria japonica*) chips collected from Kawasaki Town, Miyagi Prefecture, Japan, were milled and sieved to obtain cedarwood sawdust with a particle size of ≤600 μm (hereafter CSD), which was used as the biomass precursor. $Fe(NO_3)_3 \cdot 9H_2O$ (99.0%, Wako Pure Chemicals, Japan) was used as the graphitization catalyst. HCl (35.0–37.0%, Wako Pure Chemicals, Japan) was used to leach acid-soluble and exposed Fe-containing species from the graphitized products. Ultrapure water produced by a pure water generator (WG-220, Yamato Kagaku, Japan) was used in this experiment. Samples are designated as *X* h/m_250_*Y*D, where *X* represents the residence time during hydrothermal carbonization (h = hours, m = minutes), 250 indicates the constant reaction temperature (°C), and *Y*D denotes the number of impregnation days.

CSD catalyst impregnation

In a beaker, CSD (10 g, 600 μm) was impregnated by soaking in an aqueous $Fe(NO_3)_3 \cdot 9H_2O$ solution (40 g Fe L^{-1}, 100 mL) for 0–4 days to vary iron incorporation (separate trials). The resulting wet slurries were transferred directly to a 500 mL autoclave without drying and subjected to hydrothermal carbonization. This impregnation step was intended to promote broad Fe distribution within the biomass before catalytic graphitization.

Primary carbonization

Hydrothermal carbonization was carried out in a 500 mL stainless-steel autoclave equipped with an N_2 inlet line, pressure gauge, and temperature controller. The reactor was filled, purged repeatedly with N_2, and the internal pressure was adjusted to approximately 2 MPa. The reaction was conducted at 250 °C with stirring under 300 rpm for the desired residence time.

After cooling, the slurry was discharged and filtered through a 0.45 μm OMNIPORE™ membrane (Merck Millipore). The recovered hydrochar was washed several times with ultrapure water and dried overnight at 105 °C. The HLP was collected directly after filtration without additional dilution or washing, thereby preserving the native concentration of dissolved organics and lignin for subsequent recovery.

Secondary carbonization (catalytic graphitization)

The carbonization process was carried out using a high-temperature electric tubular furnace (FULL-TECH). The furnace temperature was controlled using a temperature controller. Nitrogen gas was supplied from a cylinder through a flow meter, and the exhaust valve was kept open throughout the process to maintain continuous flow. After HTC, 3.0 g of the dried hydrochar was placed in the furnace, and N_2 gas was supplied at 500 mL min^{-1}. The sample was heated to 1000 °C at a rate of ~16 °C min^{-1} and maintained at this temperature for 1 h. After the holding period, the furnace was allowed to cool naturally to room temperature under continuous N_2 flow.

The carbonized product (~1.5 g) was subsequently mixed with 200 mL of HCl (2 mol L^{-1}) and allowed to stand overnight to leach acid-soluble and exposed inorganic species, including Fe-containing species. The solid was recovered using a 0.45 μm OMNIPORE™ membrane (Merck Millipore), washed several times with ultrapure water, and dried overnight at 105 °C in a constant-temperature oven to obtain the biomass-derived graphitic carbon (BGC).

Air calcination

The tertiary calcination process was carried out using a high-temperature electric tubular furnace (FULL-TECH). The furnace temperature was controlled using a temperature controller. Air was supplied from a cylinder through a flow meter, and the exhaust valve was kept open throughout the process to maintain continuous flow. After acid washing and drying, 1.0 g of BGC was placed in the furnace, and air was supplied at 500 mL min^{-1}. The sample was heated to 400 °C at a rate of ~16 °C min^{-1} and maintained at this temperature for 1 h. After the holding period, the furnace was allowed to cool naturally to room temperature under continuous air flow. The process resulted in approximately 98% of the calcined, highly crystalline graphitic carbon successfully recovered.

 This journal is © The Royal Society of Chemistry 2026

Materials characterization and analysis

The BGC samples were characterized by XRD (Ultima IV, RIGAKU, Japan) using Cu Kα radiation. Baseline correction was applied to the XRD patterns prior to analysis and plotting. The Scherrer equation was used to estimate crystallite dimensions from XRD peak broadening.

The equation is as follows:

$$L = \frac{\lambda K}{\mathrm{FWHM}\cos\theta} \quad (1)$$

where L is the crystallite height (L_c) or lateral size (L_a), in nm, K is the Scherrer constant (0.91) for L_c and (1.84) for L_a, λ is the X-ray wavelength (0.15443 nm for Cu Kα_2 radiation), FWHM is the full width at half maximum of the diffraction peak; the values listed in Table 1 are in degrees and were converted to radians for the calculation, θ is the Bragg angle.

For interlayer distance (d_{002})

$$d_{002} = \frac{\lambda}{2\sin\theta} \quad (2)$$

where, d_{002} is the interlayer distance (in nm), λ is the X-ray wavelength (0.15443 nm for Cu Kα_2 radiation), θ is the Bragg angle.

Raman spectra were obtained using a RAMANforce microscope with a 532 nm excitation laser. The integrated I_D/I_G ratio was used to estimate the crystallite size (L_a) *via* the Tuinstra–Koenig relation.

$$L_a(\mathrm{nm}) = \frac{2.4\times10^{-10}\cdot\lambda^4}{I_D/I_G}$$

Microstructure was observed using TEM (HT-7500, Hitachi) and TEM-EDS (JEM-2100F, JEOL). Fe content in the hydrochar was measured using ICP-OES (Thermo iCAP 6000, 213.859 nm). The elemental composition of the raw CSD was determined by CHNSO analysis (Elementar vario EL cube) for carbon yield evaluation.

Thermogravimetric measurements were performed using a simultaneous DTA-TG analyzer (DTG-60AH, Shimadzu, Japan). For the hydrochar samples, the temperature was initially increased from 30 to 105 °C at a heating rate of 10 °C min^{-1} under an air flow of 100 mL min^{-1} and held at 105 °C for 15 min. The temperature was then increased to 1000 °C at 10 °C min^{-1}, and for the graphitized samples, the temperature was increased from 30 to 105 °C at 10 °C min^{-1} under a nitrogen flow of 100 mL min^{-1} and held at 105 °C for 15 min. The temperature was subsequently increased to 450 °C at 10 °C min^{-1} and held for 10 min, followed by heating to 900 °C at the same rate of 10 °C min^{-1}.

The Fe coordination environments of the hydrochar samples were analyzed using the Fe K-edge X-ray absorption near-edge structure (XANES) and extended X-ray absorption fine structure (EXAFS). XAFS measurements were performed at the BL-9A beamline of the Photon Factory, KEK, Ibaraki, Japan. The energy calibration was carried out using a standard Fe foil. XAFS data processing was performed using the Athena program within the Demeter software package.[83] To obtain the EXAFS radial distribution function in R-space, the extracted $\chi(k)$ functions were k^3-weighted and Fourier transformed over a k range of 3–12 $\mathrm{Å}^{-1}$

Electrode fabrication

Electrode slurries were prepared by dispersing post-air-treated BGC as active material, an acetylene black conductive agent (Denka Black, HS-100), and a polyvinylidene fluoride (PVDF) binder at an optimized mass ratio of 90 : 3 : 7 wt% in *N*-methyl-2-pyrrolidone (NMP). The mixture was homogenized for 12 h and doctor-blade coated onto a 10 μm thick copper current collector (without carbon coating) with a 300 μm wet gap clearance. After vacuum drying to eliminate residual NMP, the composite film was consolidated under a 5-ton pressing load, yielding an average active mass loading of 2.8 mg cm^{-2} and a structural electrode density of 0.66 g cm^{-3}. Circular working electrode disks were subsequently punched out for cell integration.

Electrochemical characterization

Electrochemical performance was evaluated using standard CR2032-type coin cells assembled as half-cells inside an Ar-filled glovebox (moisture/oxygen < 0.1 ppm) at 25 ± 3 °C. The punched BGC electrode disk served as the working electrode, paired against a pure metallic lithium disk reference/counter electrode and isolated by a three-layer polymeric membrane separator (UP3085). The liquid electrolyte was 1.0 mol L^{-1} $\mathrm{LiPF_6}$ in a binary solvent system of ethylene carbonate (EC) and diethyl carbonate (DEC) (1 : 1 v/v). Specific capacities were normalized to the mass of active material, and 371.9 mAh g^{-1} was used as the theoretical graphite-capacity reference.

Before the rate-capability measurements, the cells used for the rate tests underwent a three-cycle galvanostatic conditioning protocol at 0.1C. The initial-cycle data shown in Fig. 7d was obtained using separate freshly assembled cells. Due to the intrinsic diffusion resistance of the thick-film bio-graphite matrix, the initial lithiation step was governed by an extended constant current–constant voltage (CC–CV) sequence: CC lithiation at 0.1C down to 0.005 V with a maximum time limit of 30 h, followed by a CV step at 0.005 V until the current decayed to a 0.05C cutoff threshold (5 h maximum duration). After a 10 min open-circuit rest period, CC delithiation was performed at 0.1C up to an upper cutoff potential of 1.6 V (15 h maximum duration). The specific discharge capacity recorded on the 3rd conditioning cycle established the exact 1C benchmark for subsequent rate calculation.

To decouple the independent kinetic transport resistances governing lithium insertion and extraction, two separate sets of conditioned coin cells were deployed for asymmetric rate capability assessments:

Set A (lithiating kinetics): variable-current CC lithiation was applied at progressive rates (0.1C, 0.5C, 1C, 2C, 5C, and 10C; five consecutive cycles per block) down to 0.005 V, followed by a 10 min rest phase, and a fixed baseline CC delithiation at 0.1C up to 1.6 V.

Set B (delithiating kinetics): symmetric CC–CV lithiation was first conducted at a fixed baseline of 0.1C down to 0.005 V (CV

step capped at 0.05C for a maximum of 1 h). Following a 10 min rest phase, asymmetric variable-current CC delithiation was performed up to 1.6 V across the matching rate sequence (0.1C to 10C; 5 continuous cycles per block).

Cyclic voltammetry (CV) was conducted on a separate conditioned cell from its open-circuit voltage over a potential window of 0.0–1.5 V *vs.* Li/Li^+ at a constant scan rate of 0.1 mV s^{-1} for 3 continuous cycles.

Author contributions

Preethi Perianayagam: writing – original draft, visualization, validation, methodology, investigation, formal analysis, data curation. Edwin Osebe Nyangau: validation, formal analysis, writing – review & editing. Futa Imaizumi: investigation. Naoka Nagamura: formal analysis, Hideharu Niwa: formal analysis, Takashi Itoh: resources, supervision. Masaru Watanabe: project administration, methodology, writing – review & editing, supervision, resources. Yuta Nakayasu: writing – review & editing, visualization, validation, supervision, resources, project administration, methodology, funding acquisition, conceptualization.

Conflicts of interest

There are no conflicts to declare.

Data availability

Most of the data presented in this paper are included in the main manuscript, and the supplementary information (SI), and additional data are available from the corresponding author upon reasonable request. Supplementary information is available. See DOI: https://doi.org/10.1039/d6se00774k.

Acknowledgements

This work was also supported by Environment Research and Technology Development Fund (grant No. JPMEERF20223C04 and JPMEERF20263005) from the Environmental Restoration and Conservation Agency, Ministry of the Environment of Japan; the Kurita Water and Environment Foundation (KWEF) (grant no. 25A028); the Japan Society for the Promotion of Science (JSPS) KAKENHI (grant no. 25K21634); and Tohoku Initiative for Fostering Global Researchers for Interdisciplinary Sciences (TI-FRIS) under the Strategic Professional Development Program for Young Researchers of the Ministry of Education, Culture, Sports, Science and Technology (MEXT). The authors also acknowledge the generous support from FRIS CoRE, Tohoku University, a shared research facility. We thank Dr Makoto Nagasako for his support with the TEM observation and Dr Hitoshi Abe for his support with XAFS analysis. This work utilizes AI-based tools to assist with language editing and manuscript preparation. The authors take full responsibility for the content of the manuscript.

References

1 B. P. Thapaliya, A. S. Ivanov, H. Y. Chao, M. Lamm, M. Chi, H. M. Meyer, X. G. Sun, T. Aytug, S. Dai and S. M. Mahurin, *Carbon*, 2023, **212**, 118151, DOI: 10.1016/j.carbon.2023.118151.
2 S. Bhattacharyya, S. Roy, X. Lin, N. Campagnol, A. Vlad and P. M. Ajayan, *Nat. Rev. Mater.*, 2026, **11**, 65–78, DOI: 10.1038/s41578-025-00848-5.
3 M. Armand and J. M. Tarascon, *Nature*, 2008, **451**, 652–657, DOI: 10.1038/451652a.
4 D. Guerard and A. Herold, *Carbon*, 1975, **34**, 337–345, DOI: 10.1016/0008-6223(75)90040-8.
5 J. Asenbauer, T. Eisenmann, M. Kuenzel, A. Kazzazi, Z. Chen and D. Bresser, *Sustainable Energy Fuels*, 2020, **4**, 5387–5416, DOI: 10.1039/d0se00175a.
6 T. Shang, H. Zhan, Q. Gong, T. Zeng, P. Li and Z. Zeng, *Energy*, 2024, **297**, 131269, DOI: 10.1016/j.energy.2024.131269.
7 Y. Lan, X. Zhao, W. Zhang, L. Mu and S. Wang, *Energy*, 2022, **245**, 123292, DOI: 10.1016/j.energy.2022.123292.
8 M. S. Soffian, F. Z. A. Halim, F. Aziz, M. A. Rahman, M. A. M. Amin and D. N. A. Chee, *Environ. Adv.*, 2022, **9**, 100259, DOI: 10.1016/j.envadv.2022.100259.
9 W. J. Sagues, J. Yang, N. Monroe, S. Han, T. Vinzant, M. Yung, H. Jameel, M. Nimlos and S. Park, *Green Chem.*, 2020, **22**, 7093–7108, DOI: 10.1039/D0GC02286A.
10 T. Vook, S. C. Dey, J. Yang, M. Nimlos, S. Park, S. Han and W. J. Sagues, *J. Energy Storage*, 2023, **73**, 109242, DOI: 10.1016/j.est.2023.109242.
11 M. Sevilla, C. Sanchís, T. Valdés-Soh, E. Morallón and A. B. Fuertes, *J. Phys. Chem. C*, 2007, **111**, 9749–9756, DOI: 10.1021/jp072246x.
12 B. A. Lim, S. Lim, Y. L. Pang, S. H. Shuit and S. H. Kuan, *Renewable Sustainable Energy Rev.*, 2023, **184**, 113451, DOI: 10.1016/j.rser.2023.113451.
13 S. Rigollet, E. Weiss-Hortala, G. Flamant and A. Nzihou, *Chem. Eng. J.*, 2024, **496**, 153795, DOI: 10.1016/j.cej.2024.153795.
14 M. Komiyama, *Catal. Rev.*, 1985, **27**(2), 341–372, DOI: 10.1080/01614948508064738.
15 G. Domazetis, J. Liesegang and B. D. James, *Fuel Process. Technol.*, 2005, **86**(5), 463–486, DOI: 10.1016/j.fuproc.2004.03.009.
16 K. Bru, J. Blin, A. Julbe and G. Volle, *J. Anal. Appl. Pyrolysis*, 2007, **78**(2), 291–300, DOI: 10.1016/j.jaap.2006.08.006.
17 G. Cheng, H. Li, J. Fang, X. Wang, J. Li, J. Chang, N. Teng and J. Wang, *Carbon Lett.*, 2025, **35**, 441–467, DOI: 10.1007/s42823-025-00872-z.
18 S. Xia, H. Yang, W. Lu, N. Cai, H. Xiao, X. Chen, Y. Chen, X. Wang, S. Wang, P. Wu and H. Yang, *Energy*, 2022, **239**, 122262, DOI: 10.1016/j.energy.2021.122262.
19 M. A. A. Farid, A. L. T. Zheng, T. Tsubota and Y. Andou, *J. Anal. Appl. Pyrolysis*, 2023, **173**, 106064, DOI: 10.1016/j.jaap.2023.106064.

 This journal is © The Royal Society of Chemistry 2026

20 E. O. Nyangau, H. Abe, K. Haga, C. Ooka, K. Hayashida, N. Nagamura, K. Takeyasu, M. Watanabe and Y. Nakayasu, *J. Power Sources*, 2025, **653**, 237784, DOI: 10.1016/j.jpowsour.2025.237784.

21 H. Abe, Y. Nakayasu, K. Haga and M. Watanabe, *Glob. Chall.*, 2023, **7**, 2300112, DOI: 10.1002/gch2.202300112.

22 H. Jeong, J. Kim, S. Lee, D. U. Kim, J. Kim and J. Yang, *J. Alloys Compd.*, 2025, **1020**, 179485, DOI: 10.1016/j.jallcom.2025.179485.

23 H. You, J. Hui, Y. Zhou, K. Vittore, J. Zhang, L. E. Chaney, S. Chinta, Y. Zhao, G. Lim, D. Lee, E. A. Ainsworth, J. B. Dunn, V. P. Dravid, M. C. Hersam and S. J. Rowan, *Small*, 2024, **20**, 2406669, DOI: 10.1002/smll.202406669.

24 K. Jurkiewicz, B. Liszka, P. Gancarz, S. Smykała, D. Zygadło, P. Nokielski, T. Lamrani, E. Talik, R. Wrzalik, M. Walkowiak and J. Ilavsky, *Adv. Funct. Mater.*, 2024, **34**, 2410409, DOI: 10.1002/adfm.202410409.

25 L. Lower, S. M. Rowland, M. Regula, K. Iisa, Z. A. Combs, S. Park, T. Vries, T. Vries, M. R. Nimlos and W. Joe Sagues, *ChemSusChem*, 2025, **18**, e202402509, DOI: 10.1002/cssc.202402509.

26 H. Weldekidan, A. K. Mohanty and M. Misra, *ACS Environ. Au*, 2022, **2**, 510–522, DOI: 10.1021/acsenvironau.2c00029.

27 The Ministry of Agriculture, Forestry and Fisheries, Japan, https://www.rinya.maff.go.jp/j/sin_riyou/kafun/data.html, accessed March 2022.

28 N. Phaiboonsilpa, K. Yamauchi, X. Lu and S. Saka, *J. Wood Sci.*, 2010, **56**, 331–338, DOI: 10.1007/s10086-009-1099-0.

29 Y. Kurata, Y. Mori, A. Ishida, M. Nakajima, N. Ito, M. Hamada, K. Yamashita, T. Fujiwara, M. Tonosaki and Y. Katayama, *J. Wood Chem. Technol.*, 2018, **38**, 254–263, DOI: 10.1080/02773813.2018.1434206.

30 K. Murakami, K. Fuda and M. Sugai, *J. MMIJ*, 2008, **124**, 143–147, DOI: 10.2473/journalofmmij.124.143.

31 T. Yamagishi, S. Yamauchi, K. Suzuki, T. Suzuki, Y. Kurimoto, T. Takayama and Y. Sakai, *J. Wood Sci.*, 2020, **66**, 82, DOI: 10.1186/s10086-020-01930-y.

32 N. Zhang, M. C. James, S. G. Krishnan, D. A. Keiser, B. Kehoe, T. Béguerie, C. E. White and A. Nzihou, *Carbon*, 2026, **260**, 121906, DOI: 10.1016/j.carbon.2026.121906.

33 G. Davies and J. McGregor, *ACS Omega*, 2021, **6**, 33000–33009, DOI: 10.1021/acsomega.1c05116.

34 Y. Nakayasu, Y. Goto, Y. Katsuyama, T. Itoh and M. Watanabe, *Carbon Trends*, 2022, **8**, 100190, DOI: 10.1016/j.cartre.2022.100190.

35 T. Yamagishi, S. Yamauchi, S. Shibutani, H. Suzuki, T. Takayama and Y. Sakai, *J. Wood Sci.*, 2022, **68**, 7, DOI: 10.1186/s10086-022-02014-9.

36 K. Lotz, A. Wütscher, H. Düdder, C. M. Berger, C. Russo, K. Mukherjee, G. Schwaab, M. Havenith and M. Muhler, *ACS Omega*, 2019, **4**, 4448–4460, DOI: 10.1021/acsomega.8b03369.

37 A. C. Ghogia, L. M. Romero Millán, C. E. White and A. Nzihou, *ChemSusChem*, 2023, **16**, e202201864, DOI: 10.1002/cssc.202201864.

38 G. Gonnella, G. Ischia, L. Fambri and L. Fiori, *Energies*, 2022, **15**, 950, DOI: 10.3390/en15030950.

39 L. G. Cançado, K. Takai, T. Enoki, M. Endo, Y. A. Kim, H. Mizusaki, N. L. Speziali, A. Jorio and M. A. Pimenta, *Carbon*, 2008, **46**, 272–275, DOI: 10.1016/j.carbon.2007.11.015.

40 R. F. Susanti, A. A. Arie, H. Kristianto and A. Suhendi, *Ionics*, 2019, **25**, 3915–3925, DOI: 10.1007/s11581-019-02904-x.

41 E. Thompson, A. E. Danks, L. Bourgeois and Z. Schnepp, *Green Chem.*, 2015, **17**, 551–556, DOI: 10.1039/C4GC01673D.

42 R. D. Hunter, J. Ramírez-Rico and Z. Schnepp, *J. Mater. Chem. A*, 2022, **10**, 4489–4516, DOI: 10.1039/d1ta09654k.

43 Z. Sun, D. Yao, C. Cao, Z. Zhang, L. Zhang, H. Zhu, Q. Yuan and B. Yi, *J. Environ. Manage.*, 2022, **318**, 115555, DOI: 10.1016/j.jenvman.2022.115555.

44 A. Gomez-Martin, Z. Schnepp and J. Ramírez-Rico, *Chem. Mater.*, 2021, **33**, 3087–3097, DOI: 10.1021/acs.chemmater.0c04385.

45 M. Chen, L.-L. Shao, J.-J. Li, W.-J. Pei, M.-K. Chen and X.-H. Xie, *RSC Adv.*, 2016, **6**, 35228–35238, DOI: 10.1039/C6RA01408A.

46 M. T. H. Siddiqui, S. Nizamuddin, H. A. Baloch, N. M. Mubarak, D. K. Dumbre, Inamuddin, A. M. Asiri, A. W. Bhutto, M. Srinivasan and G. J. Griffin, *Environ. Chem. Lett.*, 2018, **16**, 821–844, DOI: 10.1007/s10311-018-0724-9.

47 H. Meng, Z. Chen, W. Wei, J. Xu, H. Duan, M. Zheng and B. J. Ni, *npj Mater. Sustainability*, 2025, **3**, 7, DOI: 10.1038/s44296-024-00047-3.

48 W. Yu, T. Sun, Z. Liu, J. Kou and C. Xu, *ISIJ Int.*, 2014, **54**, 56–62, DOI: 10.2355/isijinternational.54.56.

49 M. Bastide d'Izard and S. Abanades, *Chem. Eng. J. Adv.*, 2025, **24**, 100925, DOI: 10.1016/j.ceja.2025.100925.

50 H. Okudera, A. Yoshiasa, K. Murai, M. Okube, T. Takeda and S. Kikkawa, *J. Mineral. Petrol. Sci.*, 2012, **107**, 127–132, DOI: 10.2465/jmps.110624.

51 D. K. Bora, A. Braun, S. Erat, O. Safonova, T. Graule and E. C. Constable, *Curr. Appl. Phys.*, 2012, **12**, 817–825, DOI: 10.1016/j.cap.2011.11.013.

52 A. Espinosa, *et al.*, *Meas. Sci. Technol.*, 2012, **23**, 015602, DOI: 10.1088/0957-0233/23/1/015602.

53 M. Miao, S. Zuo, Y. Zhao, Y. Wang, H. Xia, C. Tan and H. Gao, *Carbon*, 2018, **140**, 504–507, DOI: 10.1016/j.carbon.2018.09.018.

54 F. Herold, S. Prosch, N. Oefner, K. Brunnengräber, O. Leubner, Y. Hermans, K. Hofmann, A. Drochner, J. P. Hofmann, W. Qi and B. J. M. Etzold, *Angew. Chem., Int. Ed.*, 2021, **60**, 5898–5906, DOI: 10.1002/anie.202014862.

55 C. Chen, K. Sun, C. Huang, M. Yang, M. Fan, A. Wang, G. Zhang, B. Li, J. Jiang, W. Xu and J. Liu, *Biochar*, 2023, **5**, 51, DOI: 10.1007/s42773-023-00229-7.

56 J. Kim, J. Kim, H. Park, Y. Kim and J. Yang, *J. Power Sources*, 2026, **663**, 238867, DOI: 10.1016/j.jpowsour.2025.238867.

57 M. Prieto, H. Yue, N. Brun, G. J. Ellis, M. Naffakh and P. S. Shuttleworth, *Polymers*, 2024, **16**, 2633, DOI: 10.3390/polym16182633.

58 B. M. Ghanim, D. S. Pandey, W. Kwapinski and J. J. Leahy, *Bioresour. Technol.*, 2016, **216**, 373–380, DOI: 10.1016/j.biortech.2016.05.087.

59 M. T. Reza, E. Rottler, L. Herklotz and B. Wirth, *Bioresour. Technol.*, 2015, **182**, 336–344, DOI: 10.1016/j.biortech.2015.02.024.
60 H. D. Pham, T. Shelley, P. K. Annamalai, J. Feldman, T. T. Nguyen, A. Helwig and A. K. Nanjundan, *Small*, 2025, **21**, e09226, DOI: 10.1002/smll.202509226.
61 J. O. Ighalo, F. C. Akaeme, J. Georgin, J. S. de Oliveira and D. S. P. Franco, *Sustainability*, 2025, **17**, 1660, DOI: 10.3390/su17041660.
62 G. Caygill, M. Zanfir and A. Gavriilidis, *Org. Process Res. Dev.*, 2006, **10**, 539–552, DOI: 10.1021/op050133a.
63 J. J. Carberry, *Ind. Eng. Chem.*, 1966, **58**, 40.
64 S. Yu, J. He, Z. Zhang, Z. Sun, M. Xie, Y. Xu, X. Bie, Q. Li, Y. Zhang, M. Sevilla, M. M. Titirici and H. Zhou, *Adv. Mater.*, 2024, **36**, 2307412, DOI: 10.1002/adma.202307412.
65 S. Rigollet, T. Béguerie, E. Weiss-Hortala, G. Flamant and A. Nzihou, *Sci. Rep.*, 2025, **15**, 6418, DOI: 10.1038/s41598-025-91204-8.
66 A. Shalaby, D. Nihtianova, P. Markov, A. D. Staneva, R. S. Iordanova and Y. B. Dimitriev, *Bulg. Chem. Commun.*, 2015, **47**, 291–295.
67 K. K. Garlapati, S. Ghosh, J. Dutta, B. B. Panigrahi and S. K. Martha, *Adv. Energy Mater.*, 2025, **15**, 2500501, DOI: 10.1002/aenm.202500501.
68 A. Wang, P. Dhamelincourt, J. Dubessy, D. Guerard, P. Landais and M. Lelaurain, *Carbon*, 1989, **27**, 209–218, DOI: 10.1016/0008-6223(89)90125-5.
69 C. Liang, Y. Chen, M. Wu, K. Wang, W. Zhang, Y. Gan, H. Huang, J. Chen, Y. Xia, J. Zhang, S. Zheng and H. Pan, *Nat. Commun.*, 2021, **12**, 119, DOI: 10.1038/s41467-020-20380-0.
70 S. C. Dey, L. Lower, T. Vook, M. N. Islam, W. J. Sagues, S. D. Han, M. R. Nimlos, S. S. Kelley and S. Park, *Green Chem.*, 2024, **26**, 8840–8853, DOI: 10.1039/D4GC01647E.
71 M. A. Pimenta, G. Dresselhaus, M. S. Dresselhaus, L. G. Cançado, A. Jorio and R. Saito, *Phys. Chem. Chem. Phys.*, 2007, **9**, 1276–1290, DOI: 10.1039/b613962k.
72 J. W. Long, M. Laskoski, T. M. Keller, K. A. Pettigrew, T. N. Zimmerman, S. B. Qadri and G. W. Peterson, *Carbon*, 2010, **48**, 501–508, DOI: 10.1016/j.carbon.2009.09.068.
73 M. Sathish, T. Tomai and I. Honma, *J. Power Sources*, 2012, **217**, 85–91, DOI: 10.1016/j.jpowsour.2012.05.099.
74 Z. Chen, D. L. Danilov, L. H. J. Raijmakers, K. Chayambuka, M. Jiang, L. Zhou, J. Zhou, R.-A. Eichel and P. H. L. Notten, *J. Power Sources*, 2021, **509**, 230345.
75 T. Xing, T. Ramireddy, L. H. Li, D. Gunzelmann, H. Zeng, W. Qi, S. Zhou and Y. Chen, *Phys. Chem. Chem. Phys.*, 2015, **17**, 5084–5089.
76 V. Sharova, A. Moretti, G. A. Giffin, D. V. Carvalho and S. Passerini, *C*, 2017, **3**, 22, DOI: 10.3390/c3030022.
77 S. C. Dey, B. J. Worfolk, W. J. Sagues, R. K. Bhardwaj, B. J. Tremolet de Villers, S. M. Rowland, M. R. Nimlos and S. Park, *Energy Fuels*, 2025, **39**, 11372–11387, DOI: 10.1021/acs.energyfuels.5c01132.
78 M. Gulas, F. Delort, R. Gilardi, G. Juri, L. Ostinelli, F. Rauscher, X. Wang and S. Zürcher, *ACS Omega*, 2026, **11**, 9435–9450, DOI: 10.1021/acsomega.5c09286.
79 F. Wang, Y. Wang, Z. Guan, J. Wei, S. He, Z. Zhong, H. Chen and P. Feng, *Sustainable Energy Fuels*, 2025, **9**, 3293–3303, DOI: 10.1039/D4SE01602E.
80 T. A. Thomas, P. Ellison, D. Nam, J. Pepas, G. Zhang, S. G. Yoon, K. A. Cavallaro, E. P. Alsaç, C. Wang, H. Chen and M. T. McDowell, *MRS Energy Sustainability*, 2026, DOI: 10.1557/s43581-026-00161-w.
81 J. Kim, D. Yu, D. Kim, J. Kim and J. Yang, *FlatChem*, 2025, **51**, 100867, DOI: 10.1016/j.flatc.2025.100867.
82 I. O. Borges, O. A. T. Dias, A. K. Nair, C. M. Da Silva, C. H. Amon, A. R. Sanadi, G. H. D. Tonoli and M. Sain, *J. Power Sources*, 2026, **668**, 239371, DOI: 10.1016/j.jpowsour.2026.239371.
83 B. Ravel and M. Newville, *J. Synchrotron Radiat.*, 2005, **12**, 537–541.

 This journal is © The Royal Society of Chemistry 2026